Green Chemistry

Electronic Supplementary Information

A Robotic Platform for High-Throughput Electrochemical Analysis of Chalcopyrite Leaching – (ESI)

D. Godfrey, J. H. Bannock, O. Kuzmina, T. Welton and T. Albrecht[a,†]

Department of Chemistry, Imperial College London

1. General Information

1.1. Platform Technical Details - Sample Address

A commercial milling platform (Heiz CNC Technik High-Z S-400T) provided the basis for platform development (fig.S2b). Each of the four stepper motors (1600 *step/rev*, Nanotec) is connected sequentially to a commercial driver board (Easydriver©) followed by a digital output port (DO) of an Arduino UNO© microprocessor board. These components comprise a customised stepper motor control box with USB 3.0 connectivity (fig.S1). The ATmega328 microcontroller is loaded with in-house custom firmware via USB using the Arduino Software (IDE)©, in order to interpret stepper motor actuation commands sent by NI LabView© (VISA instrument control palette).

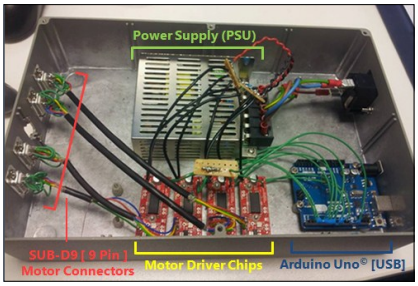

Figure S1 – Custom-built stepper motor control box based on Arduino UNO© microprocessing hardware.

Fig.S2a shows an overhead scaled technical diagram of the platform, indicating a flexible-use probe mount and laser-cut sample holder (maximum 208 vials). Manually-optimised probe positioning (**X**) is stored as a (0, 0, 0) reference position, via the upload of the aforementioned custom-built Arduino© firmware.

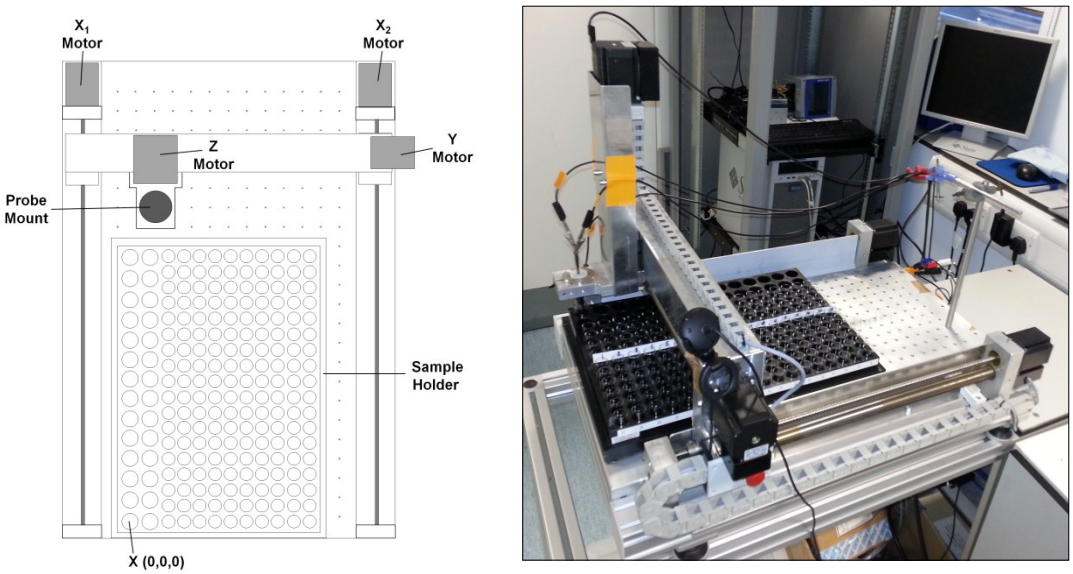

Figure S2 – a) To-scale (overhead) technical schematic of the automated robotic platform, with x,y,z motor, stored reference position (X), (180-vial) sample array and electrode mount locations highlighted. b) Photographic image of the CNC robotic platform equipped with an electrode probe, interfaced with a programmable potentiostat.

Fig.S3 summarises automated instrument workflow, highlighting that vial locations can be stored and managed from a low-level LabView© virtual instrument (vi), containing a 2-D array of vial x,y coordinates. Stepper motor revolutions are actioned through voltage pulse signals delivered to the relevant motor driver chip, for a time-step calculated by the interfacing Arduino© firmware coding, which also continuously monitors and updates current probe positioning.

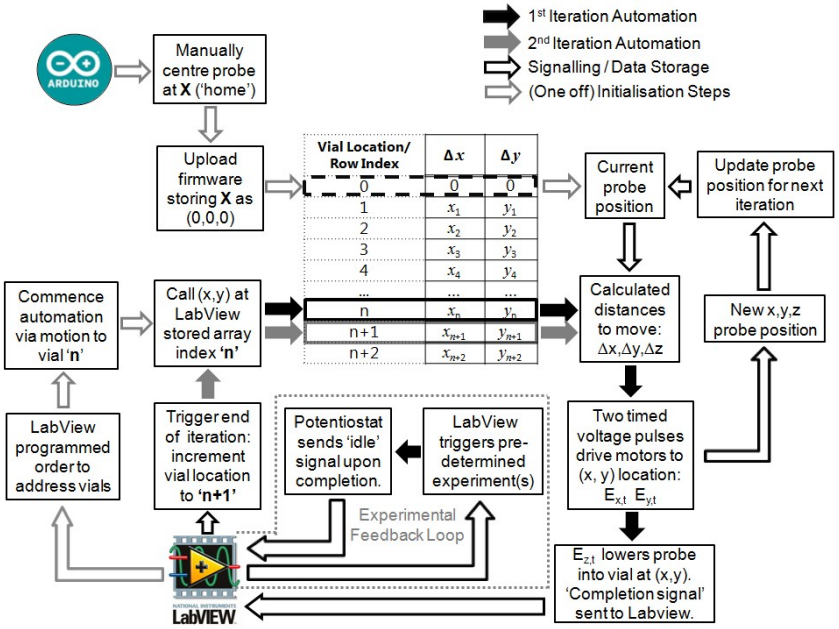

Figure S3 – Flowchart summarising the Arduino© pulsed voltage signalling of four independent stepper motors for manipulation of the probe location in x, y and z dimensions. LabView© commands interface with the Arduino© microprocessor to sequence motion and potentiostatic measurement stages.

Having successfully addressed a sample, potentiostatic electrochemistry functions (Ivium Compactstat) are accessed and sequenced in LabView via a dynamic link library (.dll). Completion of potentiostatic operations is probed through monitoring instrument status output signals, indicating the activity of the instrument and allowing triggering of the next operation. Pre-determined potentiostatic method files are executed from saved locations and further (graphical interface) coding allows data to be saved automatically – therefore, complex procedures can easily be sequenced using standard LabView functions including multistage processes and multiple procedures and repeats per sample. Dialogues in the LabView virtual instrument (vi) are set up to accept procedure-specific method files (.imf). Files with the procedure-specific parameter specifications below are designed and saved in the potentiostat software package for ease of recall (IviumSoft©).

1.2. $CuFeS_{2(s)}$ Mineral Characterisation

		% maximum theoretical concentration (109.0 *mmol.dm^{-3}*), *% (±σ)*					
Digestion ID	**ICP-AES ID**	**ICP-AES [Cu]**	**Digestion Average [Cu]**	**Overall [Cu] Average**	**ICP-AES [Fe]**	**Digestion Average [Fe]**	**Overall [Fe] Average**
Sample 1	#1	92.1 ± 0.1	92.1 ± 0.5	93.3 ± 2.8	96.3 ± 0.6	96.9 ± 0.1	96.9 ± 2.8
	#2	91.6 ± 0.4			96.2 ± 1.2		
	#3	92.6 ± 0.4			96.3 ± 1.5		
Sample 2	#1	97.0 ± 0.3	96.9 ± 0.1		100.9 ± 0.4	100.3 ± 0.6	
	#2	96.8 ± 0.2			100.2 ± 1.4		
	#3	97.0 ± 0.2			99.7 ± 0.5		
Sample 3	#1	91.2 ± 0.1	90.9 ± 0.3		94.5 ± 0.7	94.0 ± 0.7	
	#2	90.9 ± 0.2			94.5 ± 1.4		
	#3	90.6 ± 0.2			93.2 ± 1.0		

Table 1 – ICP-AES determined mineral composition summary for 200 *mg* $CuFeS_{2(s)}$ digested in 10 *mL* aquaregia (24 *hrs*; 3 $HCl_{(aq)}$: 1 $HNO_{3(aq)}$ *wt %*)

1.3. Electrochemical Techniques & Platform Validation

1.3.1. Cupric ISE Detection Limitations

Use of a commercial cupric ion selective electrode (ISE – *Cole Palmer*) was found to have significantly poorer detection capabilities in strongly coordinating $IL_{(aq)}$ media, as displayed in fig.S4. Typical response in $IL_{(aq)}$ media is characterised by a delayed onset of the Nernstian slope – raising lower detection limits to ~100 *μM* [Cu]. When accounting for noise in the analogue voltage signal there is additional precision difficulties at low [Cu], thus an alternative quantification method is required in order to monitor Cu extraction profile at low leach durations (<1 *day*). As proven in the main article, we find it possible to attain distinguishable Cu extraction data at extremely short ambient leach durations (<5 *hrs*).

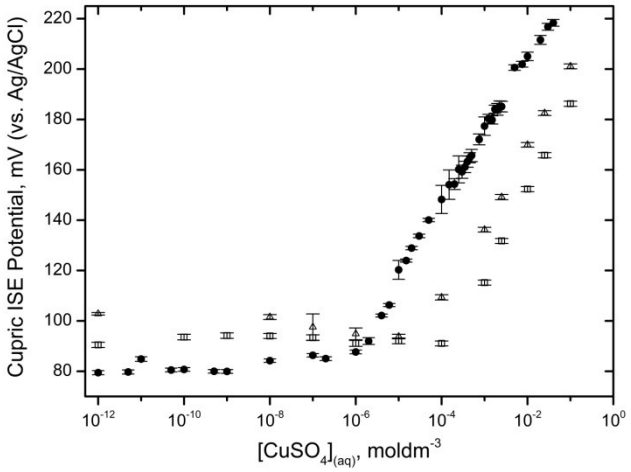

Figure S4 – Response of cupric ISE to varied $[CuSO_4]_{(aq)}$ in background 75 *mM* $[H_2SO_4]_{(aq)}$ (□), 450 *mM* $[NH_4.HSO_4]_{(aq)}$ (□) and 450 *mM* $[C_4Him][HSO_4]_{(aq)}$ (□).

1.3.2. Nernstian Dependence of Cupric ISE

$$E = E_0 - \frac{RT}{nF} ln \frac{[Red]}{[Ox]} \quad (1)$$

$$E = E_0 - 2.303 \frac{RT}{nF} log_{10} \frac{[Cu^I]}{[Cu^{II}]} \quad (2)$$

$$Cu^{2+} + e^- \rightarrow Cu^+ \qquad E_0 = 0.16V \; vs.SHE \; (0.38V \; vs.Ag/AgCl) \quad (3)$$

$$E = E_0 - 29.6 \cdot 10^{-3} log_{10} \frac{[Cu^I]}{[Cu^{II}]} \quad (4)$$

$$\Delta E = E'' - E' = 29.6 \cdot 10^{-3} log_{10} \left(\frac{[Cu^I]'}{[Cu^I]''} \cdot \frac{[Cu^{II}]''}{[Cu^{II}]'} \right) \quad (5)$$

$$\Delta E = 29.6 \cdot 10^{-3} log_{10} \left(\sim 1 \cdot \frac{[Cu^{II}]''}{[Cu^{II}]'} \right) \quad (6)$$

$$\Delta E = 29.6 \cdot 10^{-3} log_{10} \left(\frac{1}{0.1} \right) = 29.6 \; mV \quad (7)$$

1.3.3. Electrode Probe Fabrication

A glass-encased double Pt disk electrode system is fabricated by glassblowing soda glass tubes (d_{out} =5 *mm*, d_{in}=3.2 *mm*, VWR International) under a hydrogen torch to encase high purity anneal tempered Pt wires (99.99 *%*, d=1 *mm*, *Goodfellow*). Disk electrodes are revealed using SiC paper (180/320/800 *grit*, *Struers*). The Pt-glass surface is polished prior to each use (LaboPol-6, *Struers*) using a range of alumina nanoparticle suspensions (200/100/50 nm AP-A, *Struers*). Following polishing, the electrode probe is thoroughly rinsed with distilled water and electrochemically cleaned via high potential vertex cyclic voltammetry (0.5 *moldm^{-3}*

$H_2SO_{4(aq)}$, -0.4 – 1.9 *V* vs. Ag/AgCl, 100 mVs^{-1}, 10 *cycles*). Similar cleaning protocols are sequenced between the interrogation of different samples throughout this study (see exemplar trace in fig.S6 - 'Pt WE Cleaning').

1.3.4. Probe Calibration via Electrochemical Impedance Spectroscopy (EIS) Conductivity Measurements

A series of experiments were created to test platform performance and consistency. Firstly, a series of automated conductivity measurements were conducted in $KCl_{(aq)}$ and $CuSO_{4(aq)}$ via impedance spectroscopy (EIS). Impedance spectra (5 *mV* ac, 30 sampled frequencies per logarithmic decade, 1 *Hz* -1 *MHz*) are recorded using a two glass-encased Pt discs, employing one disc as a combined counter-reference electrode (vs. Pt CE/RE), after electrochemical cleaning and 60 seconds of equilibration time within each vial.

The interfacing conductive sample medium is modelled by the conventional serial combination of an Ohmic solution resistance (R_s) and a capacitive component (C_{EDL}) representing charge phenomena associated with an electric double layer. R_s values are measured at high frequencies, where capacitive behaviour diminishes according to an inverse relation to applied frequency (**8**), leaving resistive behaviour to dominate impedance response. An associated tendency of the phase angle towards 0° (degrees) is observed in the impedance response (**9**). Solution resistance values are related to solution conductivity via Ohm's law. Spectra are obtained for up to 180 samples, with unlimited repeats per sample. Total operating time for an automated two stage procedure of two repeats on 100 samples is 16.5 *hrs*, generating 200 result files.

$$[Z] = Z^{'} + Z^{''} = R_s + \frac{1}{i\omega C_{EDL}} \quad \textbf{(8)}$$

$$\varphi = arctan\left(\frac{Z''}{Z'}\right) \quad \textbf{(9)}$$

Described eis experiments were employed to validate instrument functionality and to calibrate fabricated electrode probes. Rapid, accurate Ohmic geometric factor (GF) measurements (fig.S5a and summarised in table 2) were performed for three such double Pt-disc electrodes. Solution resistance values (R_s) were extracted as described above, from impedance analysis at high frequencies for 50 samples of 1-50 *mM* $[KCl]_{(aq)}$. GF estimates were utilised to predict the conductivity of 1-50 *mM* $[CuSO_4]_{(aq)}$ solutions (**10**), reproducing cited data within error and showing excellent agreement at low $CuSO_{4(aq)}$ concentrations. Success in initial testing thus validates the platform for trial in more complex experiments, as per below.

$$R_s = GF \cdot \rho = GF.\frac{1}{\kappa} \quad \textbf{(10)}$$

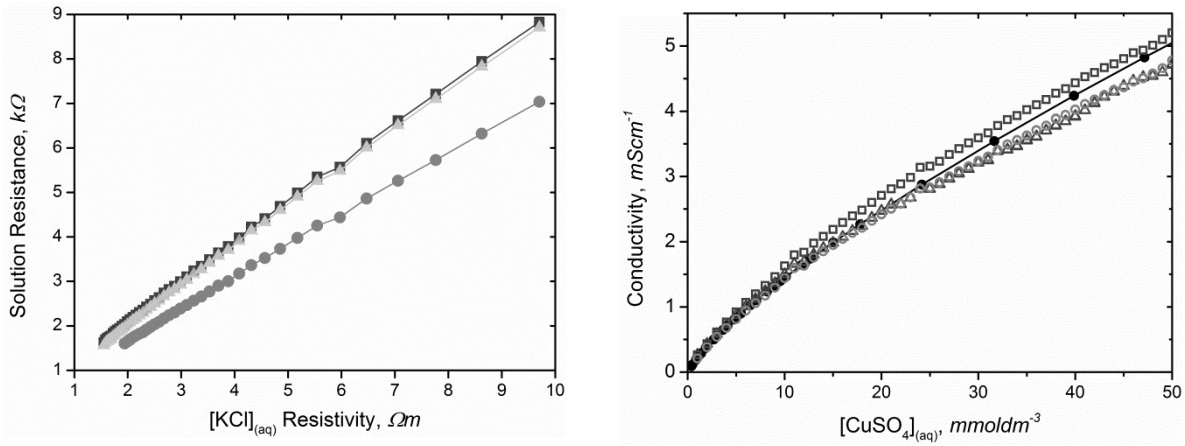

Figure S5 - a) Linear eis measured Ohmic resistance in response to varied $[KCl]_{(aq)}$ resistivity in the 1-50 *mM* concentration range, for three fabricated electrodes (□,□,□). Gradient determined geometric factors for three double-Pt disc electrodes (fabricated as described) are 889, 704 and 882 m^{-1} respectively, with <1% errors.
b) Measured conductivity of samples of 1-50 *mM* $[CuSO_4]_{(aq)}$ using determined electrode geometric factors, with all points showing ≤5% deviations from literature data for all points.

Electrode ID	Geometric Factor, m^{-1}	% Error	R^2
1	888.5	0.35	0.9995
2	704.2	0.27	0.9996
3	882.2	0.25	0.9995

Table 2 – Geometric factor measurements for three fabricated electrode systems and (Ohmic) linear slope fitting parameters.

1.3.5. Exact Procedural Design of Anodic Stripping Voltammetry (ASV)

Anodic stripping voltammetry (ASV) experiments in this study are always conducted in a 3-electrode configuration (vs. Ag/AgCl, I J Cambria). A basic procedure consists of three stages; namely CV cleaning (0.5 *M* $H_2SO_{4(aq)}$, -0.3 – 1.5 *V*, 100 mVs^{-1}, 10 *cyc*), electrodeposition in the sample medium of interest (-500 *mV*, 120 *s*) and positive polarity oxidative CV scanning (0.5 *M* $H_2SO_{4(aq)}$, -0.3 – 1.5 *V*, 50 mVs^{-1}, 4 *cycles*). Three datasets are acquired for up to 60 samples, again with unlimited repeats per sample. Total operating time for an automated three stage procedure of two repeats on 60 samples is 27hrs, generating 180 result files. Fig.S6 illustrates the aforementioned process, as used for experimentation regarding ferric remediation of copper electrodeposition, featuring the key redox transformations and highlighting the integration methods used to obtain $Cu^{II}_{(aq)}$ electrodeposition [blue] and $Cu_{(s)}$ stripping charge [red] measures. The later charge measurement process is done manually in IviumSoft© by extrapolating a chord line from the background CV trace, prior to the onset of the $Cu_{(s)}$ oxidation peak.

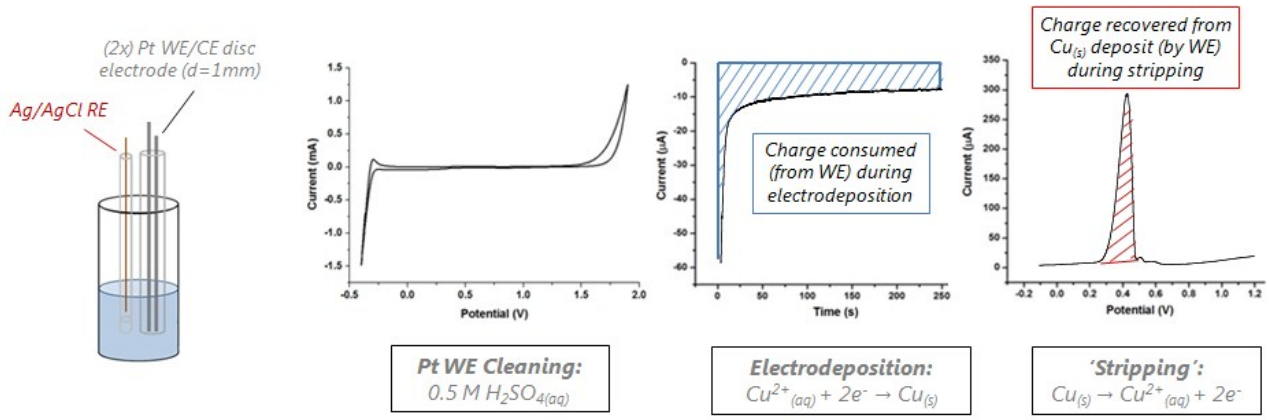

Figure S6 – Electrode configuration and exemplar electrochemical traces for 2-vial ASV. Key redox processes are indicated, alongside the charge measurement protocols used to determine the extent to which the process is occurring within a given electrolyte and electrodeposition timescale.

In the majority of experiments featured in the main experiments, a key simplification is made to the ASV procedure, enhancing experimental efficiency and minimising deviations in repeat data. Fig.S7 is a schematic representation of the key differences in the procedural approaches, caused by eliminating the separate stripping vial and conducting *back-to-back* (same sample) repeats without rigorous electrochemical cleaning. The reasoning for this choice will be explained further below.

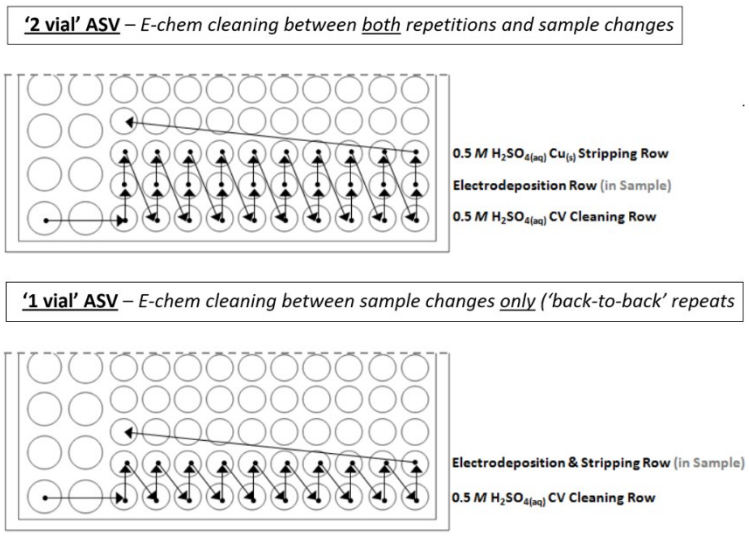

Figure S7 – Comparison of 2-vial (above) and 1-vial ASV protocols (below), using the sample holder diagram to illustrate key differences in automated motion and sequencing of electrochemical methods. For 1-vial ASV, same sample electrodeposition-stripping repeats are conducted *back-to-back* without leaving the sample vial, before moving onto the next experiment.

The regularity and necessity of electrochemical cleaning is key to automation efficiency. Fig.S8 compares measured charge for copper electrodeposition (panel a) and stripping processes (panel b) for 1-vial ASV, where unfilled data points include rigorous electrochemical cleaning between all repeats and sample changes, whereas solid markers show data for *back-to-back* repetitive

electrodeposition-stripping cycles within each sample. For the later, first repeat data comes after electrochemical cleaning and is therefore excluded from the ensuing dataset, since it shows differing behaviour. Distinct electrodeposition and stripping behaviours between the aforementioned cases are a results of complexities of the electrodeposition process, beyond the scope of this article and journal focus. However, one hypothesis is that electrochemical cleaning creates a Pt surface that is catalytically active toward proton reduction – evidenced by pH dependence of rigorously cleaned Pt electrodeposition (see table 3 for pH values) and the relative lack of medium-specific charge dependence without electrochemical cleaning.

Despite clear difference is electrodeposition-stripping characteristics, importantly, it is evident that consistency of $Cu_{(s)}$ stripping data upon repetition is not impacted by the removal of intervening electrochemical cleaning (for time-saving purposes) and actual improves linear $Cu_{(s)}$ stripping fit characteristics (table 3), strongly justifying adaptation of the process from a green perspective.

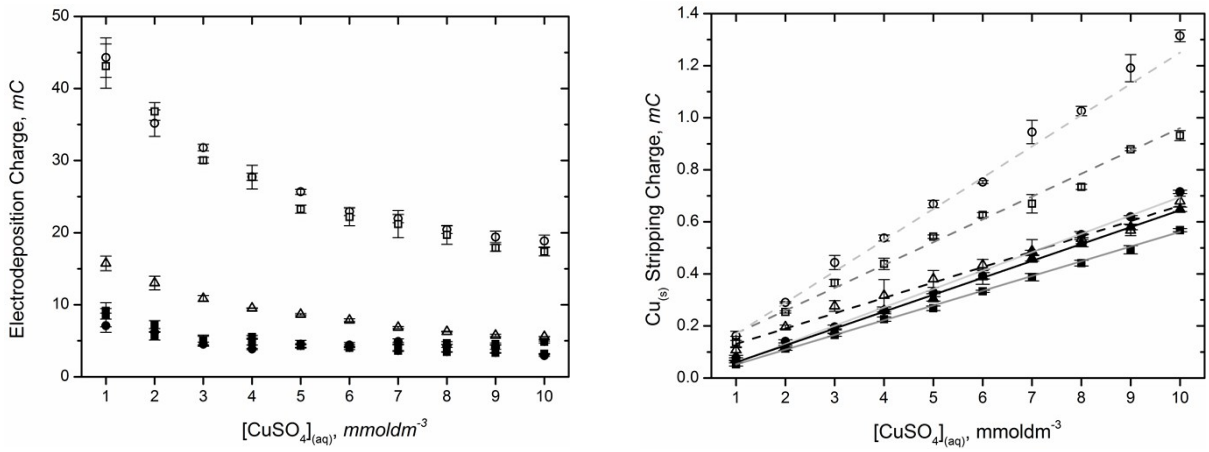

Figure S8 – Electrodeposition charge (panel a) and $Cu_{(s)}$ stripping charge data (panel b) obtained in 1-vial ASV, with (unfilled markers) and without (solid markers) the inclusion of electrochemical cleaning between sample repeats; in background 75 *mM* $H_2SO_{4(aq)}$ (□□—), 450 *mM* $[C_4Him][HSO_4]$ (□□—) and 450 *mM* $NH_4.HSO_{4(aq)}$ (□□—).

Medium	Fig.S7b ID	pH (± 0.05)	~$[H^+]$, *mM*	m, *μC mM*$^{-1}$ (σ)	c, *μC* (σ)	R^2
75 *mM* $H_2SO_{4(aq)}$	C □ ——	1.3	50.1	120 (± 2)	49.3 (± 8.2)	0.997
450 *mM* $[C_4Him][HSO_4]_{(aq)}$	C □——	1.2	63.1	59.0 (± 2.0)	71.9 (± 9.2)	0.990
450 *mM* $NH_4HSO_{4(aq)}$	C □ ——	1.0	100	87.6 (± 2.2)	84.0 (± 12.9)	0.994
75 *mM* $H_2SO_{4(aq)}$	U □ —	1.3	50.1	70.6 (± 1.4)	-11.3 (± 9.5)	0.996
450 *mM* $[C_4Him][HSO_4]_{(aq)}$	U □ —	1.2	63.1	64.9 (± 1.1)	-4.5 (± 5.3)	0.997
450 *mM* $NH_4HSO_{4(aq)}$	U □ —	1.0	100	56.6 (± 0.6)	-4.5 (± 3.1)	0.999

Table 3 - a) Calibration plot linear fit characteristics for the oxidative stripping (Pt-$Cu_{(s)}$ → $Cu^{2+}_{(aq)}$ + $2e^-$) data presented in Figure S7b, for a rigorously cleaned (C) and un-cleaned Pt-electrode (U).

Under certain experimental conditions and at high $[Cu^{2+}]$, calibration plots may plateau with repeats displaying higher standard deviations. Fig.S9 below shows this behaviour in water (□) and two concentrations of $[HNEt_3{\cdot}HSO_4]_{(aq)}$ (225 *mM* □, 450 *mM* □), thus it was considered important to maintain $Cu_{(s)}$ stripping charges within a predetermined range with close to linear response to unit variation of [Cu].

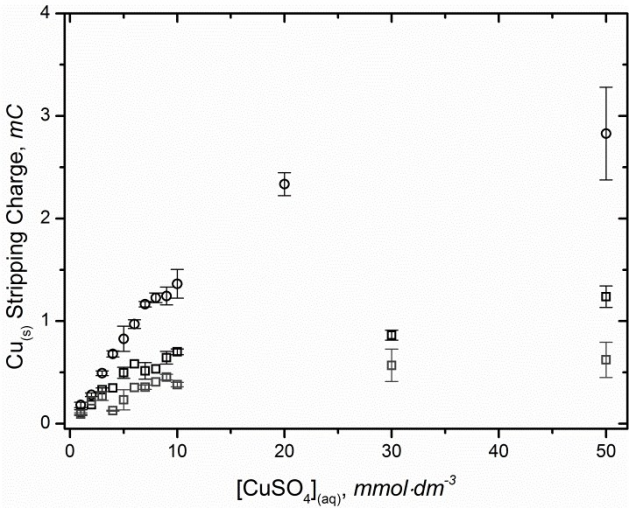

Figure 9 – ASV $Cu_{(s)}$ stripping charge calibration plots for $[CuSO_4]_{(aq)}$ in water (□) and $[HNEt_3{\cdot}HSO_4]_{(aq)}$ (225 *mM* □, 450 *mM* □) showing plateaus

1.3.6. Typical Electrodeposition Efficiencies

Hereafter, electrodeposition efficiency is defined as the charge ratio (*%*) of measured $Cu_{(s)}$ stripping charge to total electrodeposition charge, i.e. $q_{strip,Cu}$ / $q_{dep,tot}$. Fig.S10 illustrates that electrodeposition efficiency is below 1 *%* for 1 *mM* $[Cu]_{(aq)}$ in all background standard solutions studied; however, an un-cleaned Pt surface (solid markers) delivers approximately twice the electrodeposition charge efficiency of a rigorously cleaned electrode surface (open markers).

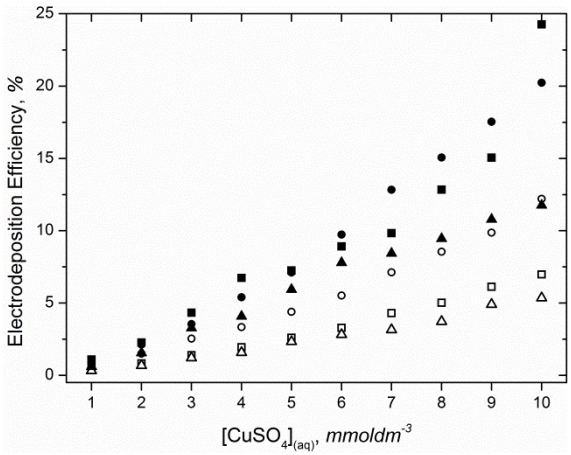

Figure S10 – Electrodeposition charge efficiencies for charge data displayed in fig.S8, comparing data obtained with a rigorously electrochemically cleaned Pt electrode surface (open markers) and an un-cleaned Pt surface (solid markers); in background 75 *mM* $H_2SO_{4(aq)}$ (□□), 450 *mM* $[C_4Him][HSO_4]$ (□□) and 450 *mM* $NH_4.HSO_{4(aq)}$ (□□).

2. Experiment Specific Information

2.1. Ferric Remediation of Cu Electrodeposition

Cupric electrodeposition has been studied extensively for the Pt-Cu system. Reported phenomena such as ferric remediation of Cu electrodeposition (using ASV) presented an excellent opportunity for platform validation, whilst utilising typical constituent species of a leach solution (H^+, Cu^{2+}, Fe^{3+}/Fe^{2+}, O_2).

2.1.1. Reconciliation of Electrodeposition Data

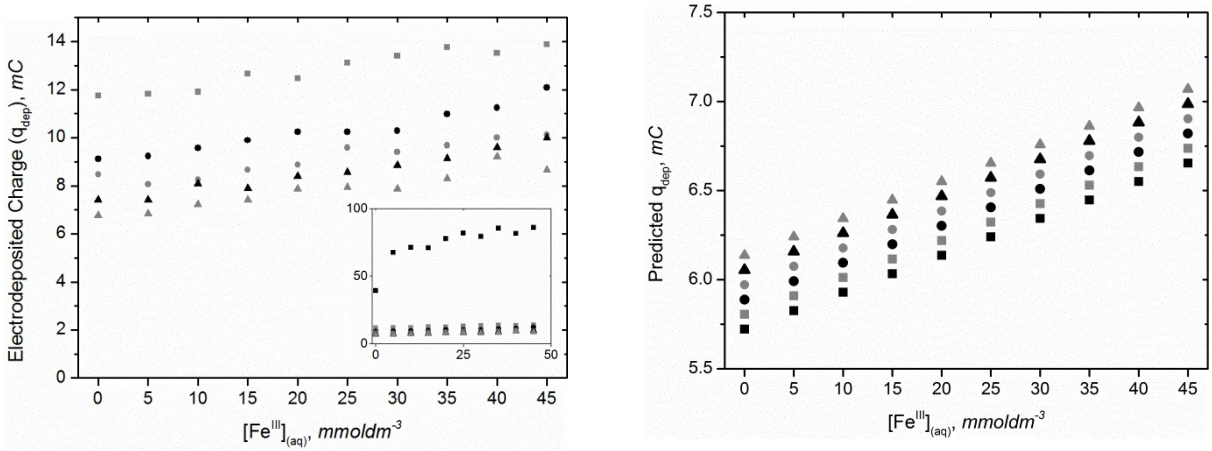

Figure S11 - a) Total electrodeposition charge data (120 *s*, -500 mV vs. Ag/AgCl) onto a 1mm diameter Pt-disc with indicated concentrations of $[Fe_2(SO_4)_3]_{(aq)}$ and with $[CuSO_4]_{(aq)}$ varied by series (□ 0 *mM* [Cu]; □ 2 *mM* [Cu]; □ 4 *mM* [Cu]; □ 6 *mM* [Cu]; □ 8 *mM* [Cu]; □ 10 *mM* [Cu]). b) Predicted charge consumption for the standard solutions used, accounting for the reduction of H^+, Cu^{2+} and Fe^{3+}.

Fig.S11b presents calculation of the predicted consumed charge during the electrodeposition cycle (120 s) formulated using the Anson equation (integrated Cottrell equation) (**11**), factoring in reduction of Cu^{2+}, Fe^{3+} and H^+ species. The predicted charge dependencies are ~41.5 $\mu C \,.\, mM\ Cu^{-1}$ and ~20.75 $\mu C \,.\, mM\ Fe^{-1}$ (0.415 *mC* and 0.933 *mC* across the full concentration ranges studied).

$$q_{dep} = \int i_{dep} \cdot dt = \int \frac{n_e FA \cdot C_0 \cdot D_0^{\frac{1}{2}}}{(\pi t)^{\frac{1}{2}}} = \frac{2n_e FA \cdot C_0 \cdot D_0^{\frac{1}{2}} \cdot t^{\frac{1}{2}}}{\pi^{\frac{1}{2}}} \quad \textbf{(11)}$$

The predicted ferric dependency is close to that observed, however the inverse trend is observed according to the cupric content of the standard, which is particularly pronounced for 0mM Cu (see Figure S5a inset). Reduction of protons is accounted for in model calculations, however rigorously electrochemically cleaned Pt surfaces are catalytically active towards $H_{2(g)}$ evolution when inserted into a low pH medium (pH 1-1.5).

The cupric concentration dependence [on charge consumed] can be better understood via the evolution of the Pt surface during the course of Cu electrodeposition. The time required to develop a non-catalytically active Pt-Cu alloyed surface varies with the inverse square of [Cu] concentration (**12**). This influence acts to reverse the theoretical trend, with the net charge varying approximately with the inverse square root of concentration. This postulate is corroborated by electrodeposition experiments in aqueous solution (Figure S7a) and equally when base is used to neutralise pH (7.0 +/- 10%), where observed consumed charge levels are on the order of 5-7 *mC*, in closer agreement with predictor models.

An alternative plot of the $Cu_{(S)}$ stripping charge associated with the discussed electrodeposition data (fig.S11a) is shown in fig.S12a. A return to expected higher measured stripping charges for higher $[CuSO_4]_{(aq)}$ content fits in well with the above hypothesis; that is, that more Cu is electrodeposited at high $[CuSO_4]_{(aq)}$ (and constant $[Fe^{III}]$), despite lower total electrodeposited charge.

$$t_{Pt-Cu} = \frac{q_{dep}^2 \cdot \pi}{(2n_e FA)^2 \cdot D_0} \cdot \frac{1}{C_0^2} \quad \textbf{(12)}$$

2.1.2. Calibration Plot Applied to Stripping Data

Fig.S12 shows the raw $Cu_{(s)}$ stripping data (panel a) and appropriate calibration plot (panel b) applicable to 120 *s* electrodeposition at -500 *mV* (vs. Ag/AgCl) with observed linear relation (**13**). The rearranged form (**14**) is used to back-calculate [Cu] concentration from stripping charge.

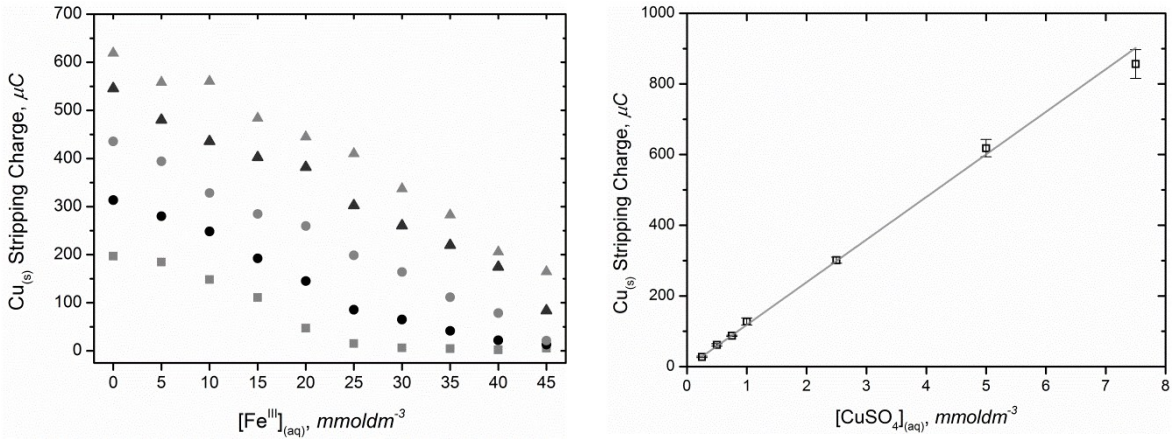

Figure S12 – a) $Fe^{III}_{(aq)}$ remediation of measured Pt-$Cu_{(s)}$ stripping charge (□ 2 *mM* [Cu]; □ 4 *mM* [Cu]; □ 6 *mM* [Cu]; □ 8 *mM* [Cu]; □ 10 *mM* [Cu]). b) Stripping charge calibration plot constructed for 120 *s* electrodeposition in $[CuSO_4]_{(aq)}$ standard solutions in background 75 *mM* $H_2SO_{4(aq)}$ applied to data from panel a to gain effective copper content. Linear fit parameters are: m = 120.5 (±2.5); c = -2.3 (±1.8); R^2 = 0.998.

$$q_{strip} = m \cdot [Cu] + c \quad \textbf{(13)}$$

$$[Cu] = \frac{q_{strip} - c}{m} \quad \textbf{(14)}$$

2.1.3. Confirmation of Iron Concentrations in Ferric Remediation Testing

ICP-AES determined [Cu] & [Fe] contents in 50 samples subjected to ASV are confirmed below in fig.S13.

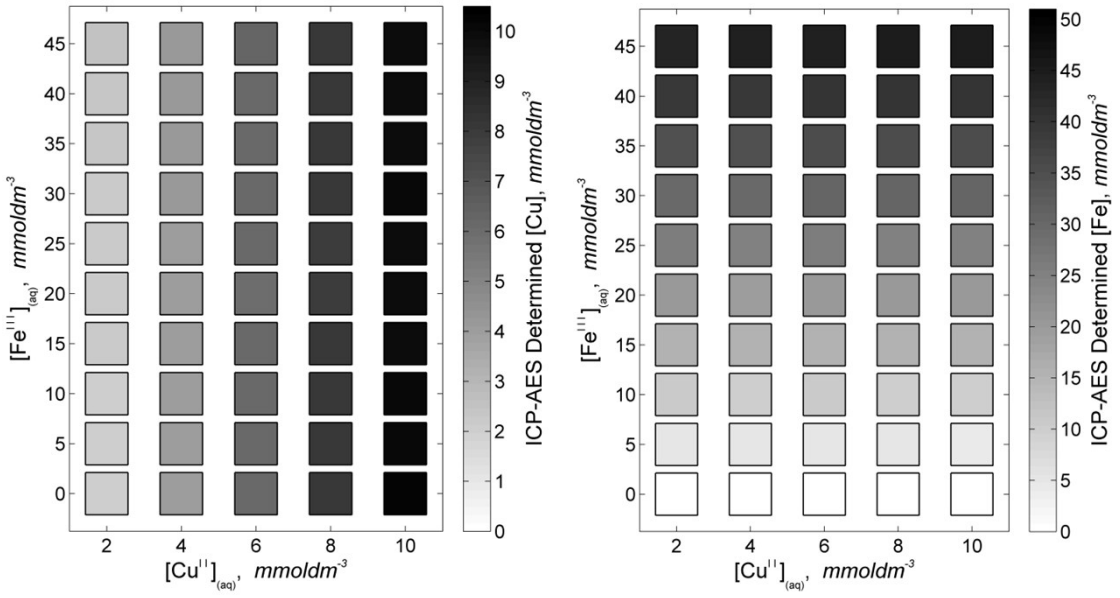

Figure S13 - ICP-AES determined metal content for copper (panel a) and iron (panel b), across a 50 vial sample array of standard solutions created using $[CuSO_4]_{(aq)}$ and $[Fe_2(SO_4)_3]_{(aq)}$.

2.1.4. Electrodeposition Efficiencies

Fig.S14 displays calculated average electrodeposition efficiencies across the 50 sample array undergoing ASV study.

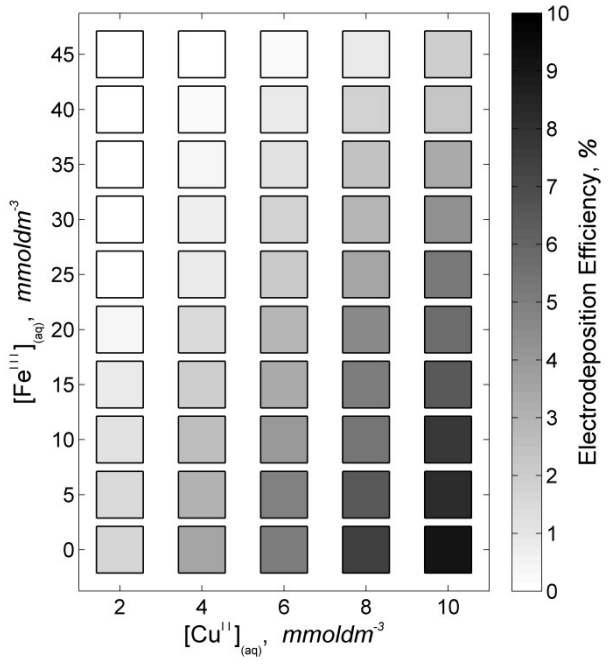

Figure S14 – Average electrodeposition efficiencies within 50 samples subjected to ASV study for ferric remediation of Cu electrodeposition.

2.2. Sample Variability Assessed Under Equal Leaching Conditions

2.2.1. Full Electrochemical Results

Fig.S15 details the full electrochemical results returned by automated ASV repetitions conducted after 72, 120 and 216 *hrs* of leaching. Four repeats of stripping data has been split into the preconditioning first cycle (R1 – fig.S15a) and later repeats (R2-4 – fig.S15b). Group statistics are described in table 4 and resultant [Cu] estimates (obtained by applying calibration in Section 2.2.3) are

discussed in the main text. Group relative variances are shown to be generally lower for repeats 2-4, as further exemplified by fig.S15.

t, *hrs*	Repeat ID	$Cu_{(s)}$ Stripping Charge, *μC*		Relative Variance (Var/Av)
		Average	Standard Deviation	
72	R1	149	± 15 (10.1 %)	1.5 x10^{-12}
	R2-4	51.5	± 4.7 (9.13 %)	4.3 x10^{-13}
120	R1	200	± 16 (8.00 %)	1.3 x10^{-12}
	R2-4	60.8	± 8.8 (14.5%)	1.3 x10^{-12}
216	R1	324	± 31 (9.57 %)	3.0 x10^{-12}
	R2-4	110	± 12 (10.9%)	1.2 x10^{-12}

Table 4 – Group statistics for electrochemical data featured in fig.S15

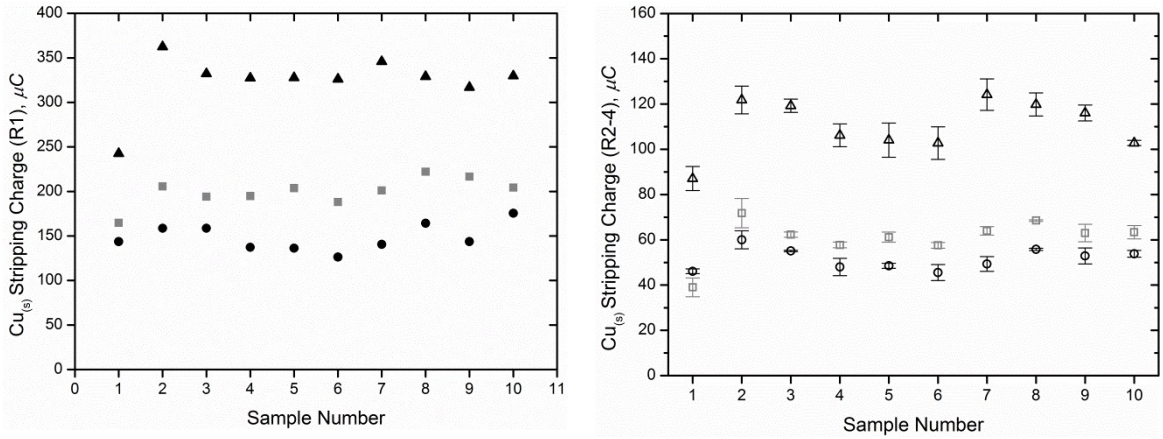

Figure S15 – Full electrochemical ASV $Cu_{(s)}$ stripping results for automated experiments conducted after 72 (□), 120 (□) and 216 *hrs* (□) of $CuFeS_{2(s)}$ leaching by 450 *mM* $[NH_4HSO_4]_{(aq)}$, split into first repeat data (R1 – panel a) and subsequent converged repeats (R2-4 – panel b).

2.2.2. $Cu_{(s)}$ Stripping Charge Normalised by ICP-AES [Cu]Concentration

For rigour, $Cu_{(s)}$ stripping data points in fig.S15 were normalised by their ICP-AES determined [Cu] content, producing values for stripping charge per molar [Cu] concentration within the sample undergoing electrodeposition (fig.S16). New data is (effectively) normalised for constant leaching timescale and data for repeats 2-4 converges to a single value, 59 ±5 $mC.mol^{-1}dm^3$, showing close agreement with the calibration coefficient output of Section 2.2.3 (56.6 $\mu C.mol^{-1}$) for the appropriate ASV parameters. This process reinforces the idea that a single calibration can be effectively applied to the raw (R2-4) data with minimal error incurred ($\sigma^2_{rel,R2\text{-}4}$ = 4.3x10^{-4}), whereas the large spread in normalised first repeat data infers that application of a single calibration coefficient will incur significant error with an order of magnitude increase in relative data variance ($\sigma^2_{rel,R1}$ = 1.6x10^{-3}).

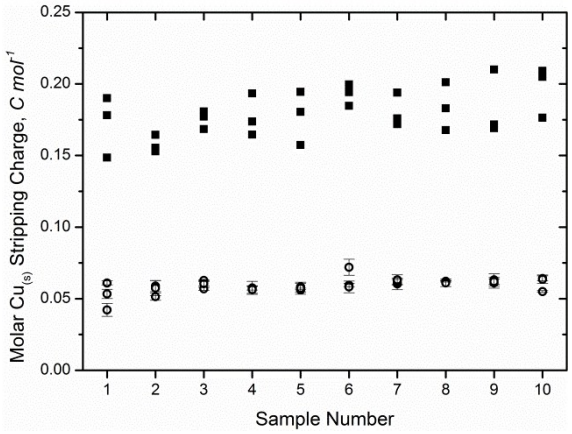

Figure S16 – (ICP-AES) [Cu] concentration normalised molar $Cu_{(s)}$ stripping charge data (**fig.S5**) separated into first repeat ASV data (□) and repeats 2-4 (□).

2.2.3. Calibration Data Applied to Stripping Data (1-vial ASV)

Using 1-10 *mM* $[CuSO_4]_{(aq)}$ standard solutions, a $Cu_{(s)}$ stripping charge calibration was obtained for the relevant 1-vial ASV electrodeposition parameters used to produce the raw stripping data described in fig.S17 (120 *s*; -500 *mV* vs. Ag/AgCl). Linear fits were applied to the stripping data (fig.S17b) and the fit parameters have been summarised in table 5. A large relative slope error (12.6 *%*) is seen for the fit applied to first repeat data, where low slope error is seen for preconditioned data (1.1 *%*), making the later slope value an excellent calibration coefficient for [Cu] estimation.

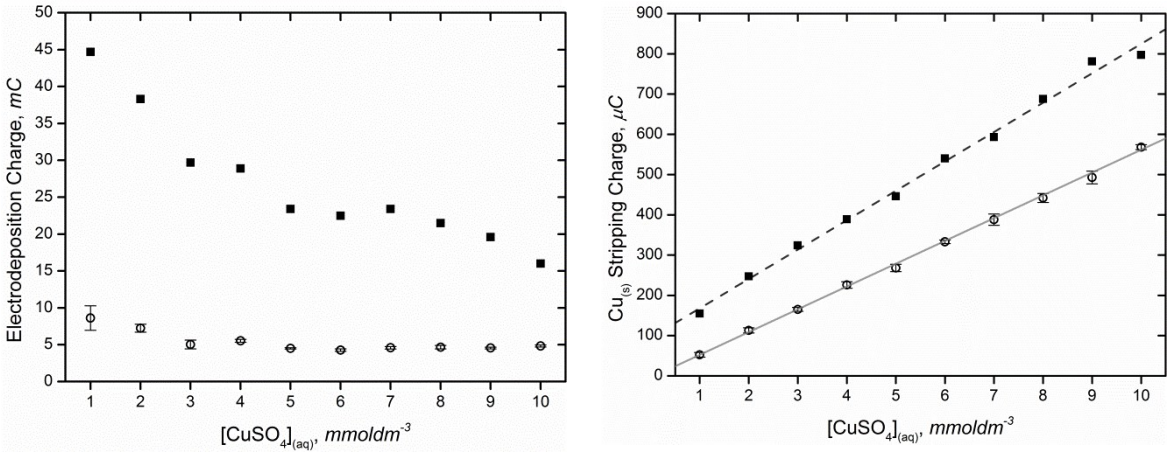

Figure S17 – Electrodeposition (panel a; 120 *s*; -500 *mV* vs. Ag/AgCl) and $Cu_{(s)}$ stripping data (panel b) for 1-vial ASV on 1-10 *mM* $[CuSO_4]_{(aq)}$ standard solutions. First repeat data (□) is separated from repeats 2-4 (□) in each plot.

Medium	Repeat ID	m, *μC mM*$^{-1}$ (σ)	c, *μC* (σ)	R^2
450 *mM* $NH_4HSO_{4(aq)}$	R1 (□ - - -)	94.6 (± 11.9)	73.0 (± 1.9)	0.9938
	R2-4 (□ —)	56.6 (± 0.6)	-4.5 (± 3.1)	0.9996

Table 5 – Linear fit characteristics and errors for the $Cu_{(s)}$ stripping data featured in **fig.S17b**.

2.2.4. ICP-AES Determined Leached [Cu] & [Fe] Concentrations

Full ICP-AES metal concentration data for 10 samples leached under equivalent conditions are shown in fig.S18 with dataset statistics summarised in table 6.

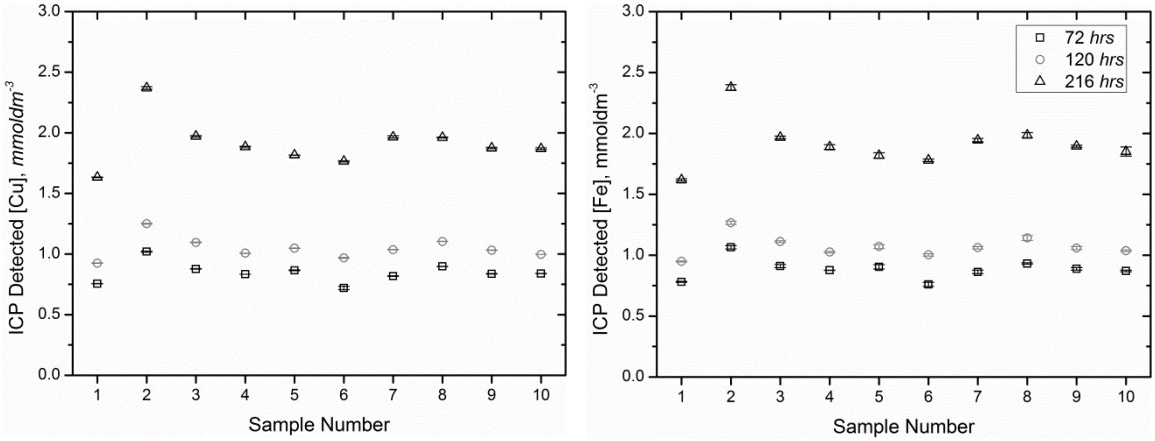

Figure S18 – ICP-AES determined [Cu] (panel a) and [Fe] (panel b) from samples taken at 72 (□), 120 (□) and 216 *hrs* (□) for 10 samples leaching under equal conditions.

t, hrs	$[M]_{av}$ ± σ (rel. σ²), *mmol.dm*$^{-3}$		
	ICP-AES [Fe]	ICP-AES [Cu]	ASV [Cu]

72	0.89 ± 0.08 (0.78 %)	0.85 ± 0.08 (0.78 %)	0.99 ± 0.08 (0.71 %)
120	1.07 ± 0.09 (0.70 %)	1.05 ± 0.09 (0.77 %)	1.15 ± 0.16 (2.10 %)
216	1.91 ± 0.20 (1.99 %)	1.91 ± 0.19 (1.92 %)	2.03 ± 0.21 (2.11 %)

Table 6 – Summary of ICP-AES metal content statistics for 72, 120 and 216 *hrs* leaching (as in fig.S18) with comparison to parallel ASV-derived [Cu] measurements

2.3. Proof-of-principle Multivariate $IL_{(aq)}$ Screening Test

2.3.1. Leachate Composition Summary

Sample Number	Sample Composition		
	$[NH_4.HSO_4]_{(aq)}$, *mM* (± 1 *mM*)	$CuFeS_{2(s)}$, *mg* (± 1 *mg*)	Volume: Mass Ratio, $mL.g^{-1}$ (± 3 %)
1	100	37.5	80
2	100	75	40
3	100	150	20
4	100	300	10
5	100	600	5
6	225	37.5	80
7	225	75	40
8	225	150	20
9	225	300	10
10	225	600	5
11	450	37.5	80
12	450	75	40
13	450	150	20
14	450	300	10
15	450	600	5
16	900	37.5	80
17	900	75	40
18	900	150	20
19	900	300	10
20	900	600	5
21	1800	37.5	80
22	1800	75	40
23	1800	150	20
24	1800	300	10
25	1800	600	5

Table 7 – Sample composition for the 25 samples leached simultaneously in a 5x5 array and studied electrochemically at 72, 164 and 216 *hrs* and subjected to ICP-AES metal content quantification at 216 *hrs*.

2.3.2. Full Electrochemical ASV Results

Samples with the compositions described in table 7 were leached for a total of 216 *hrs*, with automated electrochemical (1-vial) ASV repeats being conducted after 72, 164 and 216 *hrs* and (filtered) ICP-AES samples also obtained after 216 *hrs.* Fig.S19 details full electrodeposition and $Cu_{(s)}$ stripping charge data for the described electrochemical experiments, grouped into time-wise datasets.

Highest electrodeposition charges are observed for high ionic strength 1800 *mM* $[NH_4.HSO_4]_{(aq)}$, in agreement with the previously discussed electrodeposition pH dependencies. Within single samples, total electrodeposition charge can be observed to decrease as leaching time extends (note: constant 100 *mC* y-axis maximum), in accordance with Cu electrodeposition becoming increasingly prominent within electrodeposition timescales. Stripping results are discussed in the main text and 216 *hrs* leaching ASV results are discussed further, in reference to their corresponding ICP-AES determined [Cu] content, in Section 2.3.4 below.

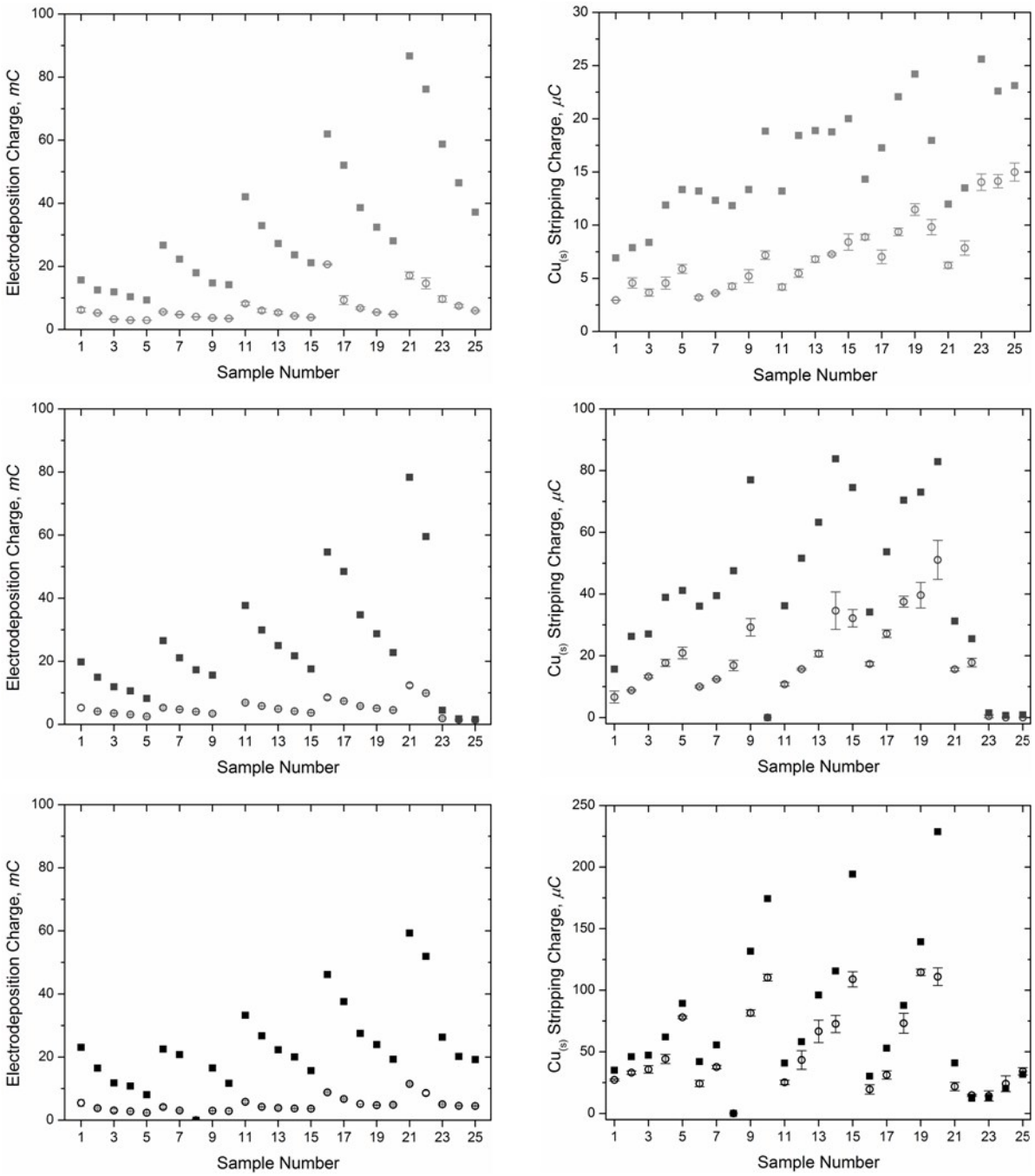

Figure S19 – Total electrodeposition charge (panel a-c) and $Cu_{(s)}$ stripping charge data (panel d-f) for 5x5 array screening assay. ASV results obtained are shown for 72 (light grey), 164 (dark grey), 216 *hrs* (black) continuous ambient leaching with repeat 1 (□) and repeats 2-4 (□) displayed separately.

2.3.3. ICP-AES Metal Concentrations and Extraction Efficiencies

After 216 *hrs* continuous leaching of the aforementioned 5x5 array, filtered ICP-AES samples were removed and analysed for [Cu] and [Fe] concentration (fig.S20a). Due to the range of $CuFeS_{2(s)}$ mass: $NH_4.HSO_{4(aq)}$ volume ratios sampled, raw ICP-AES concentration data can also be usefully represented in terms of theoretical leaching efficiency (fig.S20b) – note: this plot features no error bars, since extremely large error bars arise for low measured leaching efficiencies.

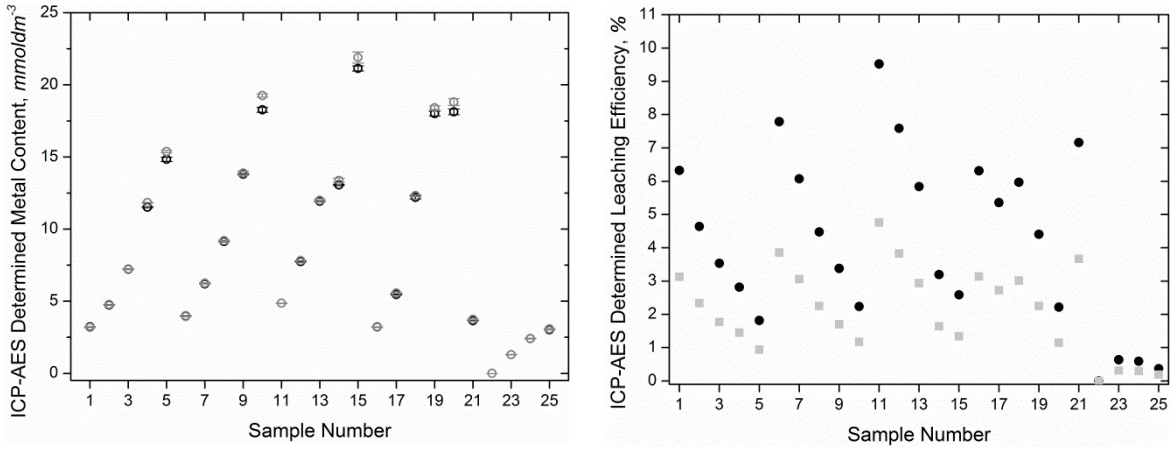

Figure S20 – ICP-AES determined [Cu] (□) and [Fe] (□) concentrations (panel a) and corresponding leaching efficiencies (panel b) across the described 25 sample array (table 6-7) after 216 *hrs* of ambient, unstirred leaching.

2.3.4. Extended Technique Correlation Plots

Fig.S14b clearly illustrates that $Cu_{(s)}$ stripping charge calibration plots have intrinsic leachate composition dependencies – showing particular sensitivity to rigor of Pt surface cleansing and leachate ion transport properties, as previously highlighted in Section 1.3.5. Since various $[NH_4HSO_4]_{(aq)}$ compositions are used across the chosen array, in the strictest sense, calibration plots should be determined for each concentration utilised, in order to back-calculate concentrations estimates with maximum accuracy.

When only treating later repeat (preconditioned) data, fig.S8b also shows that medium-specific calibration dependencies are vastly reduced – therefore it was decided to apply the assumption that the single calibration for 450 *mM* $[NH_4HSO_4]_{(aq)}$ and 120 *s* electrodeposition computed previously (Section 2.2.3 and table 5) could be applied, incurring low error. Fig.S21 and regression summary table 8, show close to unity independent measurement correlation slopes with high regression coefficients, where first repeat estimates (□) are improved upon by preconditioned repeat data (□).

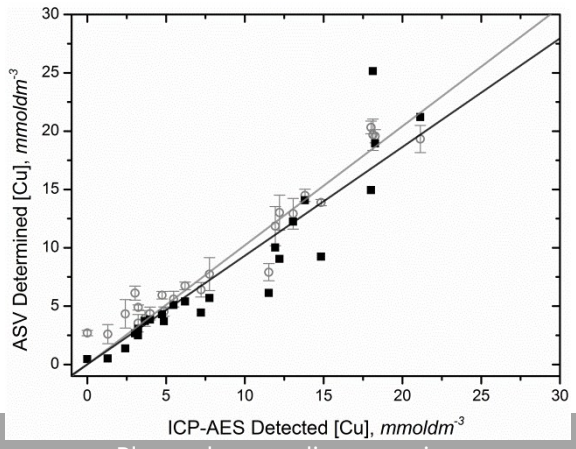

Figure S21 – Correlation plot for independent electrochemical and spectroscopic Cu measurement techniques.
Note: y-intercept values have been fixed at 0 and linear best fit parameters, plus standard errors, are summarised in table 7.

Medium	Repeat ID	m (σ)	R^2
100-1800 *mM* $NH_4HSO_{4(aq)}$	R1 (□ —)	0.93 (± 0.05)	0.943
	R2-4 (□ —)	1.02 (± 0.04)	0.963

Table 8 – Linear fit parameters for the fixed (zero) intercept regression lines featured in **fig.S21**.

2.4. In-situ Electrochemical [Cu] Leaching Sensor

Freshly milled $CuFeS_{2(s)}$ (3 *g*; 32 ≤ x ≤ 75 *μm*) was leached in stirred $[NH_4.HSO_4]_{(aq)}$ leachate solution (450 $mmoldm^{-3}$; 120 *mL*) at room temperature, with 120 *rpm* stirring. The electrode probe was prepared by fine-grain grinding, polishing with alumina suspensions; followed by 10 cycles of electrochemical CV cleaning. The cleansed probe was then preconditioned using five ASV repetitions in a 10 *mM* $[CuSO_4]_{(aq)}$, 450 *mM* $[NH_4.HSO_4]_{(aq)}$ standard solution. An automated schedule of ASV repeats at 2 *hr* intervals (without electrochemical cleaning) was designed using LabView and started immediately prior to putting the $CuFeS_{2(s)}$ particulate matter in contact with the leachate solution.

2.4.1. Experimental Setup

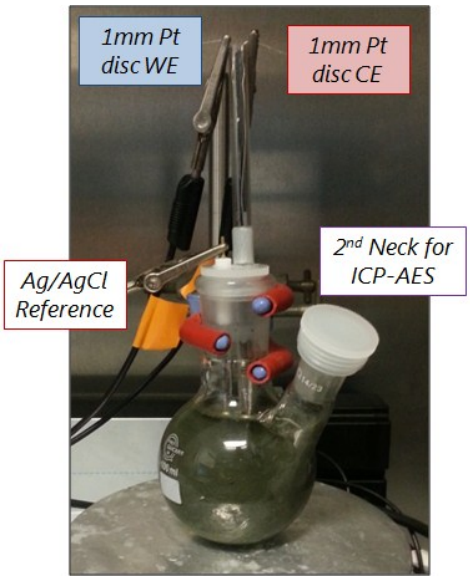

Figure S22 - Experimental setup for *in-situ* electrochemical Cu leaching sensor, including electrode assignments.

2.4.2. *In-situ* Sensing of 450 *mM* $[NH_4.HSO_4]_{(aq)}$ Leaching

2.4.2.1. Raw Electrodeposition and Stripping Data

Total electrodeposition charge data acquired for ASV cycles during the described *in-situ* Cu leaching detection experiment is displayed in fig.S23, on linear and logarithmic charge axes respectively. Large deviations are seen between first repeat ASV data and clustered data for repeats 2 and 3, similarly to previous discussion of preconditioning, despite the absence of an electrochemical CV cleaning stage, percentage reduction in total charge appears dependent upon electrodeposition timescale and remains fairly consistent within constant timescale datasets. Fig.S23a (intuitively) suggests that halving of electrodeposition timescale leads to subsequent halving of total charge, with this effect applicable to both repeat 1 data and later repeat clustered data. Further discussion of the origin of electrodeposition phenomenon is beyond the scope of the article and may be addressed by future studies.

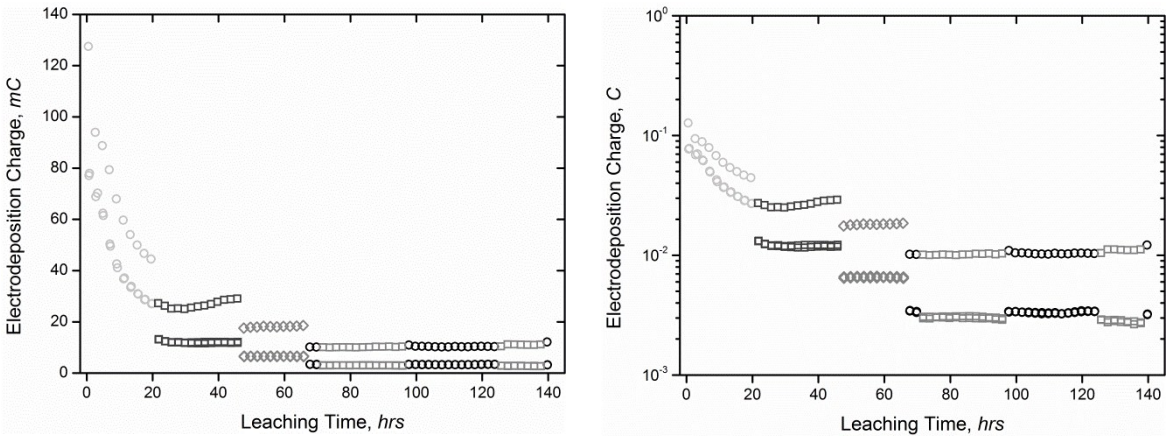

Figure S23 – a) Raw electrodeposition data collected over 140 *hrs* of $CuFeS_2$ leaching with 0.45 *mM* $[NH_4.HSO_4]_{(aq)}$ in the described setup (fig.S22) using a static *in-situ* electrode probe. b) as panel a, represented on a $\log_{10}$ charge axis (300 *s* □, 120 *s* □, 60 *s* □, 30 *s* □, 30 *s* [unstirred] □).

Paired $Cu_{(s)}$ stripping data is displayed in fig.S24, showing both raw stripping data (panel a) and normalised data (panel b) obtained by normalising charge for the lowest electrodeposition timescale of 30 *s*. As expected, repeat data disparity carries through from preceding electrodeposition. Interestingly, in terms of absolute charge, clustered later stripping data shows higher electrodeposition efficiencies in stirred conditions, whereas first repeat data shows higher efficiencies in unstirred conditions – possibly offering some insight into the causal origin of preconditioning effects observed throughout this study.

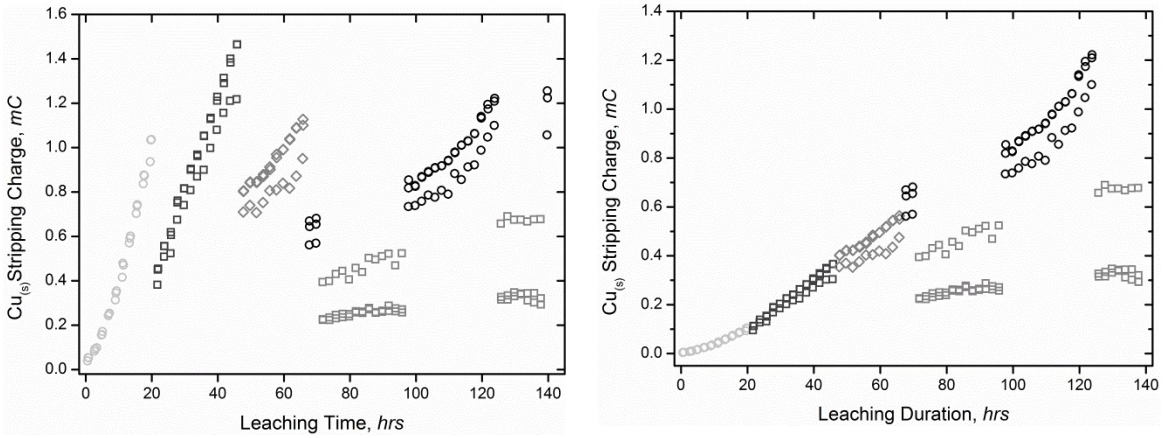

Figure S24 – a) Raw $Cu_{(s)}$ stripping data for the described *in-situ* leaching experiment, returned after the variable electrodeposition timescale cycles featured in fig23**.** b) Data from panel a, normalised to the shortest electrodeposition timescale of 30 *s*, forming a rate representative curve.

2.4.2.2. 30 *s* Electrodeposition Calibration Plot

A stripping charge calibration plot applicable to 30 *s* electrodeposition in unstirred solution was produced using 1-10 *mM* $[CuSO_4]_{(aq)}$ standard solutions in background 450 *mM* $[NH_4.HSO_4]_{(aq)}$, as displayed in fig.S25. Interestingly, under these electrodeposition conditions, preconditioned calibration plot data (fig.S25b - □) is clearly non-linear and requires fitting with a 2nd order polynomial (ax^2+bx+c). Best fit equations and parameters are summarised in table 9, with the result of back-calculation to [Cu] concentration and subsequent implications being discussed in depth in the main text.

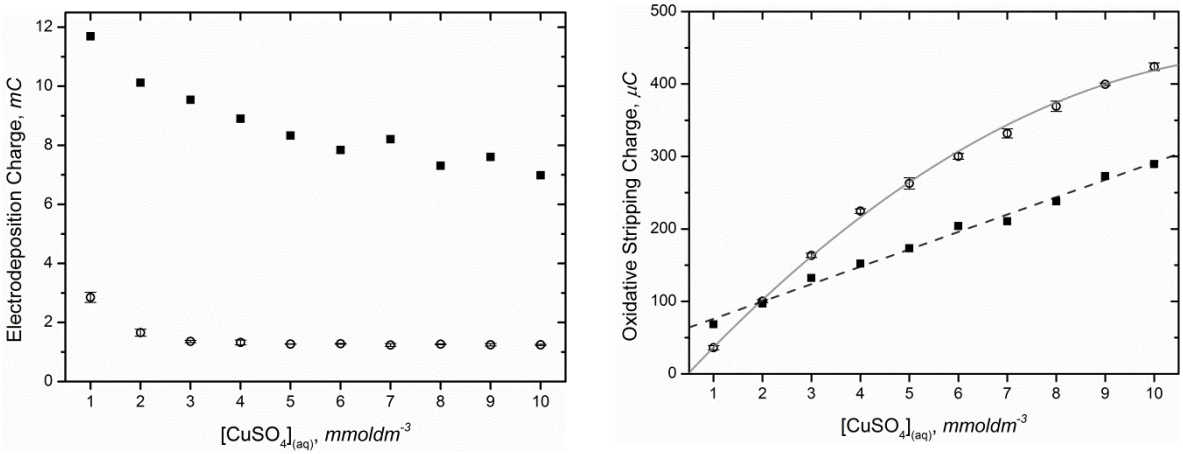

Figure S25 – ASV electrodeposition data (panel a) and $Cu_{(s)}$ stripping charge calibration plot (panel b) applicable to 30 *s* electrodeposition (-500 *mV* vs Ag/AgCl) in an unstirred vessel, as applied to the relevant raw stripping data obtained using the described *in-situ* online leaching sensor.

			Fitting Parameters, x10^{-6}			
Medium	**Repeat ID**	**Fit Equation**	**a (σ)**	**b (σ)**	**c (σ)**	**R²**
450 *mM* $NH_4HSO_{4(aq)}$	R1 (□ - - -)	y = b.x + c	n/a	24.0 (± 0.8)	51.9 (± 4.7)	0.991
	R2-4 (□—)	$y = a.x^2 + b.x + c$	-2.9 (± 0.3)	74.3 (± 2.9)	-35.0 (± 5.7)	0.999

Table 9 - Best fit parameter summary for the $Cu_{(s)}$ stripping charge data displayed in **Fig.S25**.

2.4.2.3. Electrodeposition Efficiency during Leaching

Fig.S26a shows the variation of electrodeposition efficiency for automated ASV repetitions during 140 *hrs* of leaching using electrodeposition and $Cu_{(s)}$ stripping data shown above, in fig.S23a and fig.S24a respectively. Electrodeposition efficiency rises in accordance with increasing [Cu] concentrations as seen in ICP-AES determined metal content (fig.S26b and fig.5b in main article). Uniform increases in electrodeposition efficiency are only broken by switching off the stirring between ~70-97 *hrs* and ~125-138 *hrs*.

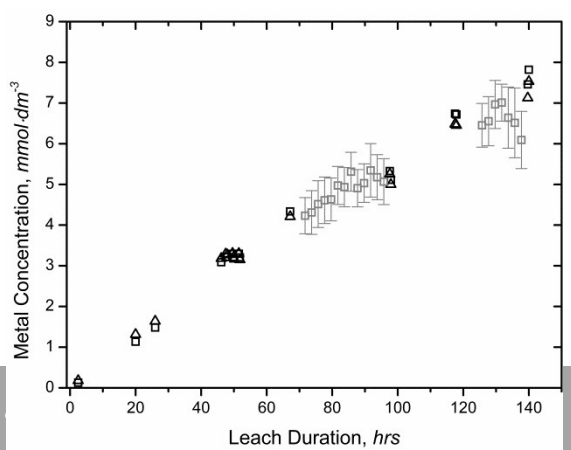

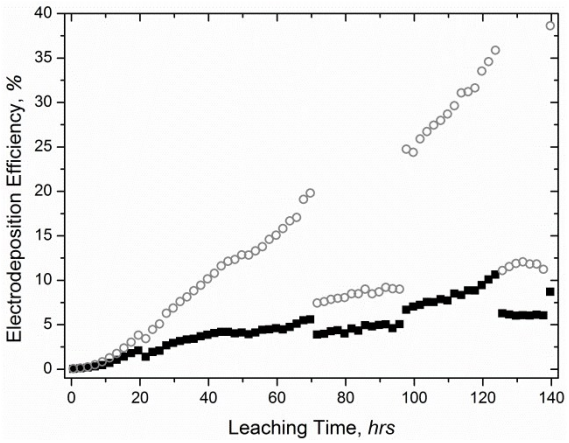

Figure S26 – a) Electrodeposition efficiency for first repeat (□) and the average efficiency for repeats 2-3 (□) constructed from raw (unnormalised) data returned by the *in-situ* leaching sensor during 140 *hrs* of leaching in 450 *mM* $[NH_4HSO_4]_{(aq)}$, as described above.
b) Mid-leach ICP-AES determined copper (□) and iron (□) concentrations, including copper concentrations measured independently via ASV data obtaining for 30 *s* electrodeposition, under unstirred conditions (□).

2.4.3. Monitoring 450 *mM* $[C_4Him][HSO_4]_{(aq)}$ Leaching

2.4.3.1. Raw Electrodeposition and Stripping Data

Fig.S27 below displays the electrodeposition data acquired over approximately 600 hours of leaching, recorded for 450 *mmol.dm*$^{-3}$ $[C_4HIm][HSO_4]_{(aq)}$ in analogous fashion to Section 2.4.2 (120 *mL*, 3 *g* $CuFeS_{2(s)}$). On account of the slower rate of leaching and differing solution transport properties, only 300 *s* and 120 *s* electrodeposition time (-500 *mV* vs. Ag/AgCl) were appropriate for use.

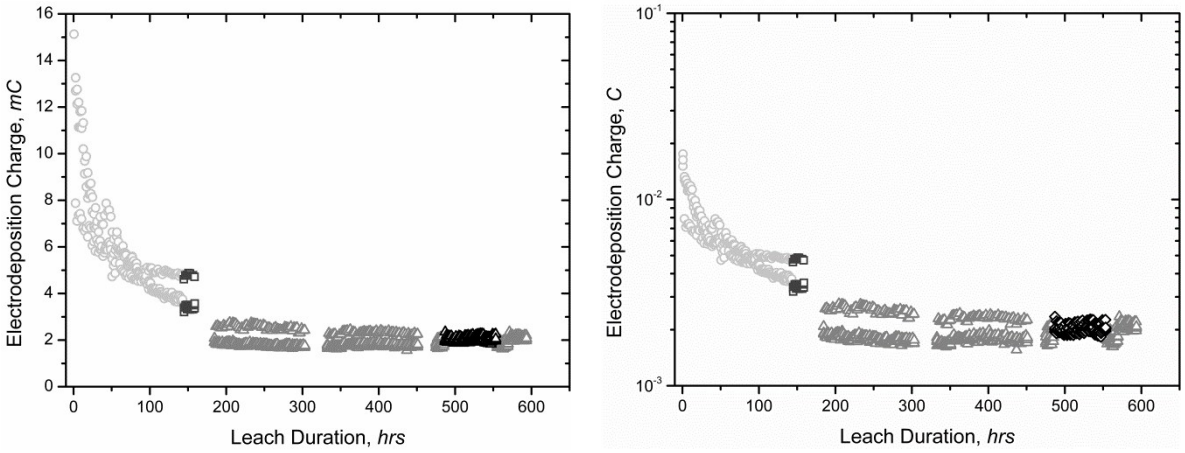

Figure S27 – a) Raw electrodeposition data collected over 600 *hrs* of $CuFeS_2$ leaching for 0.45 *mM* $[C_4Him][HSO_4]_{(aq)}$ in the described setup (**fig.S22**) using a static *in-situ* electrode probe. b) as panel a, represented on a $\log_{10}$ charge axis (300 *s* [stirred] □, 300 *s* [unstirred] □, 120 *s* [unstirred] □, 120 *s* [stirred] □).

The corresponding $Cu_{(s)}$ stripping data is featured in fig.S28. Below 40 *hrs* there is little distinguishable leaching activity, after which, similar electrochemical response is observed to that of $NH_4.HSO_4$ albeit with observation of vastly reduced charges. Datasets generally contain significantly more noise than for $NH_4.HSO_4$, which is accounted for by the necessary use of longer electrodeposition durations to provide meaningful data – however the formation of a parabolic cupric extraction profile can be observed from panel b where charges are normalised to the shortest electrodeposition timescale of 120 *s*.

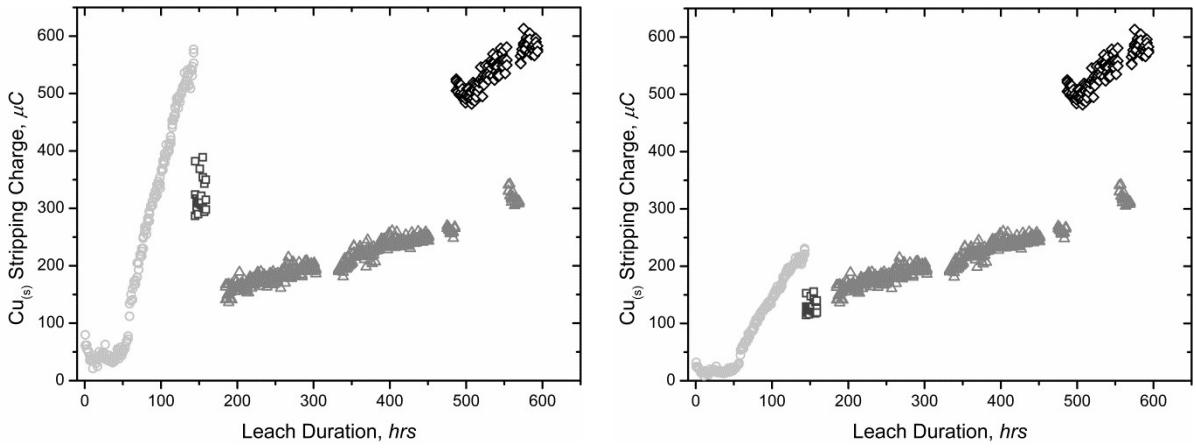

Figure S28 – a) Raw $Cu_{(s)}$ stripping data for the described 0.45 moldm^{-3} $[C_4Him][HSO_4]_{(aq)}$ *in-situ* leaching experiment, returned after the variable electrodeposition timescale cycles featured in **fig27.** b) Data from panel a, normalised to the shortest electrodeposition timescale of 120 *s*, forming a rate representative curve.

2.4.3.2. 300 *s* and 120 *s* Electrodeposition Calibration Plots

ASV charge calibration plots were created for unstirred 120 *s* and 300 *s* electrodeposition, to provide electrochemical [Cu] measurements from raw $Cu_{(s)}$ stripping data shown in fig.S28. Parabolic and linear best fit parameters respectively have been applied to $Cu_{(s)}$ stripping charge data, the summary of which is given below in table 10.

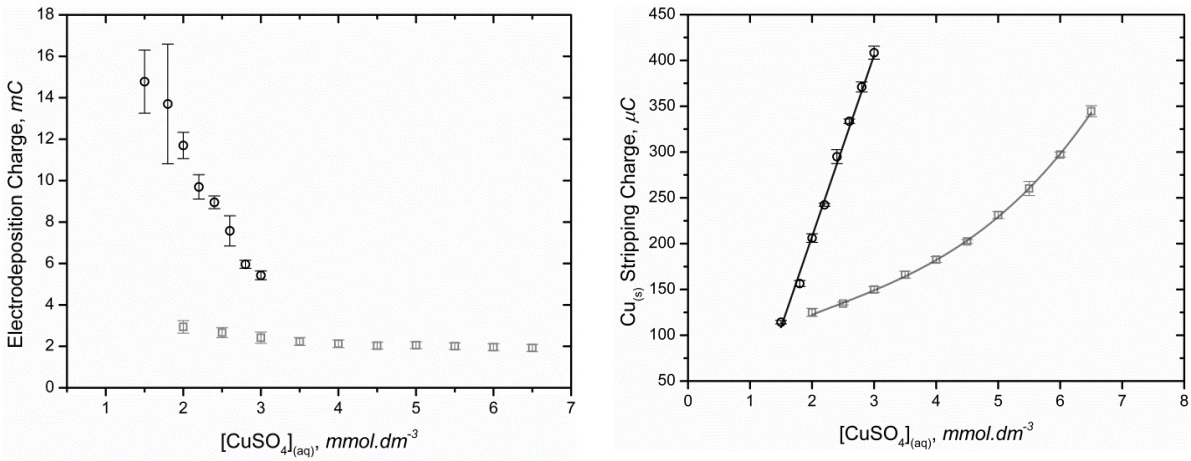

Figure S29 – Electrodeposition charge (left) and $Cu_{(s)}$ stripping charge (right) data for 300 *s* (□) and 120 *s* (□) unstirred electrodeposition in dilute $[CuSO_4]_{(aq)}$ standard solutions.

			Fitting Parameters, x10^{-6}			
Medium	**Calibration**	**Fit Equation**	**a (σ)**	**b (σ)**	**c (σ)**	**R^2**
450 *mM*	300 *s* (□)	y = b.x + c	n/a	198.0 (± 6.1)	-188.3 (± 12.9)	0.993
$[C_4Him][HSO_4]_{(aq)}$	120 *s* (□)	y = a.x^2 + b.x + c	7.9 (± 0.6)	-20.9 (± 4.6)	137.6 (± 8.6)	0.998

Table 10 - Best fit parameter summary for the $Cu_{(s)}$ stripping charge data displayed in fig.S29b**.**

2.4.3.3. Electrodeposition Efficiency during Leaching

Fig.S30a below indicates the development of electrodeposition efficiency throughout the course of 600 *hrs* of leaching in 450 *mM* $[C_4Him][HSO_4]_{(aq)}$. In contrast to the analogous plot for 450 *mM* $[NH_4.HSO_4]_{(aq)}$ (fig.S26) there is little discernable difference in electrodeposition efficiency between first repeat ASV and subsequent back-to-back repeats. However, electrodeposition efficiency reaches similar magnitudes on account of the comparable [Cu] composition (~6 *mM*) at the respective conclusion of leachate monitoring.

Applying the calibrations from Section 2.4.3.2 results in electrochemical [Cu] measurements (- fig.S30b), which can be correlated to ICP-AES [Cu] ( ) and [Fe] ( ) measurements. Independent [Cu] measures show good visual overlay, confirming a parabolic extraction profile. Interestingly, in the case of 450 *mM* $[C_4Him][HSO_4]_{(aq)}$, Fe extraction is observed at increased levels (table 11), which appear to converge to ~133 *%* of [Cu] extraction at equivalent times.

Leach Duration, *hrs*	$[M]_{av}$ ± rel.σ, *mmol.dm⁻³*		Relative Fe Extraction, *%*
	ICP-AES [Cu]	ICP-AES [Fe]	
146	2.41 ± 0.17 *%*	3.92 ± 0.41 *%*	162.5 ± 1.3 *%*
486	5.31 ± 0.09 *%*	7.10 ± 0.96 *%*	133.8 ± 1.9 *%*
555	5.58 ± 0.09 *%*	7.29 ± 0.82 *%*	130.7 ± 1.5 *%*
571	5.60 ± 0.43 *%*	7.47 ± 1.12 *%*	133.3 ± 2.5 *%*
642	6.19 ± 0.21 *%*	8.20 ± 0.78 *%*	132.4 ± 1.6 *%*

Table 11 – Summary of ICP-AES [Cu] and [Fe] measured extraction and relative Fe extraction with respect to Cu extraction.

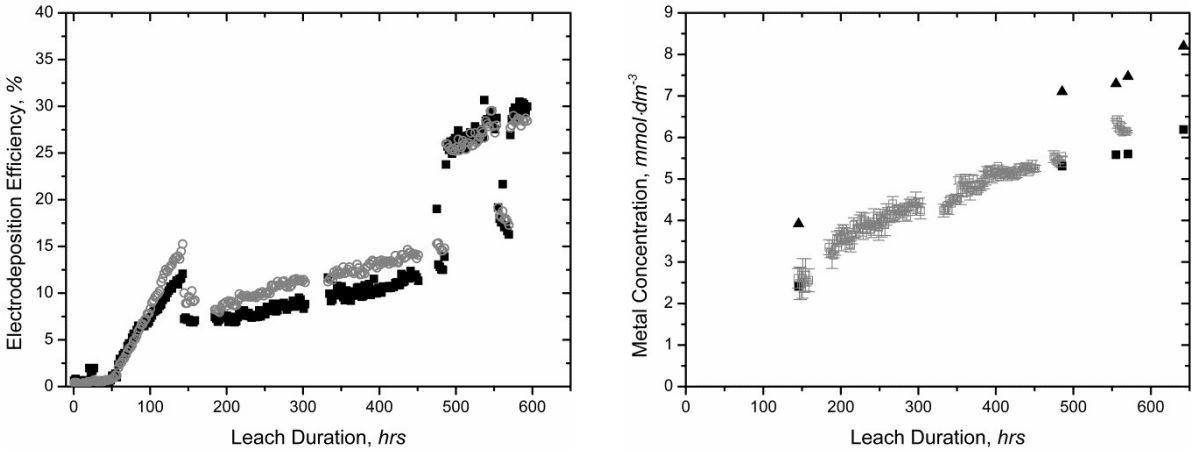

Figure S30 – a) Development of electrodeposition efficiency in 0.45 mol.dm^{-3} $[C_4Him][HSO_4]_{(aq)}$ during 600 *hrs* $CuFeS_{2(s)}$ leaching for first repeat ASV ( ) and subsequent back-to-back repeats ( ) .
b) Cu ( ) and Fe ( ) ICP-AES sampling and the corresponding electrochemical [Cu] measurements ( ) calculated from unstirred ASV data.

2.5. 24 *hr* Cu Leaching in Various $IL_{(aq)}$ Systems

The effect of IL concentration on Cu extraction from $CuFeS_2$ was investigated at 70 *°C* with 500 *rpm stirring*, with ICP-AES sampling after 24 *hrs* yielding the results in fig.S31a. Additionally, the pH of lixiviant solutions where studied at 298 *K* and ambient pressure (fig.S31b).

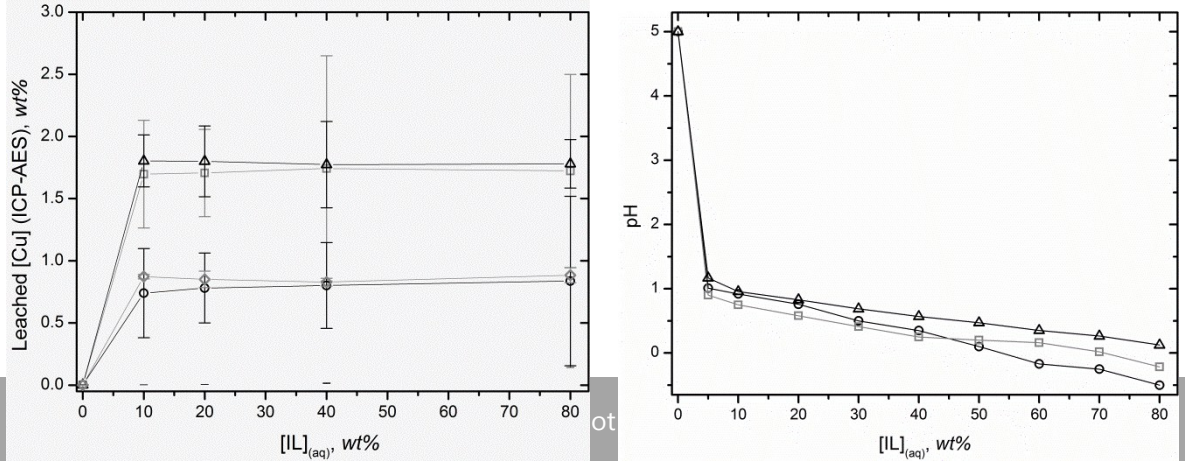

Figure S31 – Leached Cu after 24 *hrs* as a function of the *%wt* concentration of five $IL_{(aq)}$ systems (panel a) and the respective solution pH's of three $IL_{(aq)}$ across the 0-80 *wt%* concentration range - □ [HHIm][HSO_4] □$EtNH_3{\cdot}HSO_4$ □ [C_4Him][HSO_4] □ [C_4C_1Im][HSO_4].